Journal of Alloys and Compounds 900 (2022) 163457

Contents lists available at ScienceDirect

Journal of Alloys and Compounds

journal homepage: www.elsevier.com/locate/jalcom

Growth and reaction mechanism of solution-processed $Cu_2ZnSnSe_4$ thin films for realising efficient photovoltaic applications

Ersan Y. Muslih[a,l,m,*], Khan Sobayel Bin Rafiq[b,k,**], Mohammad Ismail Hossain[c], Md. Shahiduzzaman[d], Mohammad Junaebur Rashid[e], Tasmiat Rahman[f], Badrul Munir[g], Khaled Althubeiti[h], Hend I. Alkhammash[i], Huda Abdullah[j], K. Techato[k], Md. Akhtaruzzaman[b,***], Kim Kyoo Ho[l]

[a] Mechanical Engineering Department, Faculty of Industrial Technology, Trisakti University, Jakarta 11440, Indonesia
[b] Solar Energy Research Institute, The National University of Malaysia, 43600 Bangi, Selangor, Malaysia
[c] Department of Electrical and Computer Engineering, University of California, Davis, CA 95616, USA
[d] Nanomaterials Research Institute, Kanazawa University, Kakuma, Kanazawa 920-1192, Japan
[e] Department of Electrical and Electronic Engineering, University of Dhaka, Dhaka 1000, Bangladesh
[f] School of Electronics and Computer Science, University of Southampton, SO171BJ, UK
[g] Department of Metallurgy and Materials Engineering, University Indonesia, Depok, Indonesia
[h] Department of Chemistry, College of Science, Taif University, P.O. Box 11099, Taif 21944, Saudi Arabia
[i] Department of Electrical Engineering, College of Engineering, Taif University, P.O. Box 11099, Taif 21944, Saudi Arabia
[j] Department of Electrical, Electronic and Systems Engineering, Faculty of Engineering and Built Environment, Universiti Kebangsaan Malaysia, 43600 Bangi, Selangor, Malaysia
[k] Environmental Assessment and Technology for Hazardous Waste Management Research Centre, Faculty of Environmental Management, Prince of Songkla University, 90110 Songkhla, Thailand
[l] School of Material Science and Engineering, Yeungnam University, 214-1 Daedong, Gyeongsan, Gyeongbuk 712-749, South Korea
[m] Graduate School of Natural Science and Technology, Kanazawa University, Kakuma, Kanazawa 920-1292, Japan

ARTICLE INFO

Article history:
Received 14 October 2021
Received in revised form 22 December 2021
Accepted 23 December 2021
Available online 28 December 2021

Keywords:
CZTSe
Nonhydrazine
Solution process
SCAPS
FDTD

ABSTRACT

This article reports on $Cu_2ZnSnSe_4$ (CZTSe) thin film preparation via a nonhydrazine, nonpyridine and environmentally friendly low-cost solution process method. CZTSe fabrication through a solution-based process has not yet been suitably demonstrated given the impediments to addressing the presence of selenium in solutions. In this study, we introduced a two-step CZTSe fabrication method that used monoethanolamine as the chelating agent/co-solvent and ethanol as the main solvent. Selenization was then conducted. In this process, we successfully avoided the use of hydrazine to synthesise CZTSe thin films. Material characterisations (e.g. UV–VIS–NIR, scanning electron microscopy, electron dispersive spectroscopy, X-ray diffractometry and Fourier transform infrared spectroscopy) confirmed the high quality of the deposited thin films. The deposited CZTSe thin film showed high crystallinity without carbon residues, indicating its potential application as a photovoltaic absorber. Hence, we investigated the photovoltaic parameters of the CZTSe-based solar cells on the basis of the deposited thin film's optoelectronic properties. We utilised Solar Cell Capacitance Simulator to examine the electrical effects of CZTSe solar cells and used three-dimensional finite-difference time-domain optical simulations to investigate the optics of the solar cells. We estimated that the realistic power conversion efficiency of the CZTSe solar cells could reach 18.5% with a short-circuit current density of 30 mA/cm^2.

1. Introduction

Materials for photovoltaic applications have been intensively developed and shown remarkable performance. Perovskite solar cells (25.5%), silicon-based solar cells (26.7%), copper indium gallium selenide-based solar cells (22.9%), cadmium telluride-based solar cells (22.1%) and kesterite solar cells (KSCs) are the most prominent

* Corresponding author at: Mechanical Engineering Department, Faculty of Industrial Technology, Trisakti University, Jakarta 11440, Indonesia.
** Corresponding author at: Solar Energy Research Institute, The National University of Malaysia, 43600 Bangi, Selangor, Malaysia.
*** Corresponding author.
E-mail addresses: ersan.ym@trisakti.ac.id (E.Y. Muslih), sobayel@ukm.edu.my (K.S. Bin Rafiq), akhtar@ukm.edu.my (Md. Akhtaruzzaman).

https://doi.org/10.1016/j.jallcom.2021.163457
0925-8388/

photovoltaics given their power conversion efficiency (PCE) [1–4]. KSCs, such as Cu_2ZnSnS_4 (CZTS), $Cu_2ZnSnSe_4$ (CZTSe) and $Cu_2ZnSn(S,Se)_4$, are widespread in the photovoltaic community due to their simple processing [5–8]. Selenide or sulphur-based (CZTS/Se) materials are amongst the most interesting developed materials. The PCE of CZTS solar cells fabricated through evaporation can reach 11.01% [5]. The PCEs of CZTSe and CZTSSe solar cells produced through hydrazine addition are 10.54% and 12.6%, respectively [6,7]. The record efficiency of CZTSe solar cells has recently exceeded 13%, which can further allow the use of such materials for high-efficiency photovoltaics [8–13]. The recombination effect at device interfaces can be reduced via structural optimisation, thus facilitating the realisation of high-efficiency single-junction and tandem solar cells [14–17]. Thin films for CZTSe solar cells can also be prepared through thermal evaporation, sputtering, electrodeposition and solution processing [18–25]. Moreover, highly efficient CZTSe solar cells can be fabricated via the hydrazine solution process [6,25]. Hydrazine is a noncarbon organic compound that can act as the solvent of many organic or inorganic compounds [26]. Given its unique property, hydrazine is a prominent solvent for the synthesis of selenium-based kesterite films (e.g. CZTSe) that can provide large grains, increase uniformity and decrease raw material wastage [26–28]. However, deposition by using a hydrazine solvent has several drawbacks, such as flammability, corrosiveness, acute toxicity, carcinogenicity and environmental hazards [28–32]. In addition, hydrazine is a volatile compound that requires rigorous safety protocols. The vapour of pure hydrazine may explode if ignited and is incompatible with several materials, including numerous plastics and metals [17–19]. These drawbacks restrict the use of pure hydrazine in large-scale production. Process temperature, especially the temperature of postannealing treatment, reduces defects in the crystal lattice and improves the crystallinity of CZTSe thin films [33]. However, high-temperature postdeposition annealing mainly deteriorates the performance of CZTSe devices [32,34]. Annealing temperature plays an important role in the defect engineering of CZTSe thin films [25,28,34,35].

In the present study, we aimed to prepare a high-quality CZTSe thin film for efficient photovoltaic applications. In the first part of this study, a two-step reaction method was used to fabricate CZTSe thin films on glass substrates. The Cu, Zn, Sn (CZT) film precursor was prepared from metal salts (Cu^{2+}, Zn^{2+} and Sn^{4+}) in monoethanolamine (MEA). The ethanol solvent mixture was annealed at 200 °C for 15 min under ambient atmosphere. Next, selenium was added to the CZT film precursor via selenization under an Ar (95%) + H_2 (5%) atmosphere at 550 °C for 120 min. Necessary optical, electrical and structural characterisations (e.g. UV–VIS–NIR, scanning electron microscopy [SEM], energy dispersive X-ray spectroscopy [EDX], X-ray diffractometer [XRD] and Fourier transform infrared [FTIR]) confirmed the high quality of the deposited CZTSe thin films. In the second part of this study, the optoelectronic properties of the CZTSe solar cells were investigated via numerical simulations. The experimentally obtained optical and electronic values of the deposited CZTSe thin films were used as the input for numerical device modelling and simulations. Solar Cell Capacitance Simulator (SCAPS) simulations were performed to examine the electrical characteristics of the solar cells. The optics and optimisation of the devices were investigated via finite-difference time-domain (FDTD) simulations in three dimensions [4,36,37].

2. Experimental details

2.1. Soda-lime glass preparation

Soda-lime glass (SLG) was cleaned with acetone, ethanol and deionised water in an ultrasonic water bath for 20 min

2.2. Preparation of the CZT film precursor

The first step in the two-step method was the preparation of a CZT solution precursor from Cu^{2+}, Zn^{2+} and Sn^{4+} metal salts by using MEA ethanol as the mixed solvent. MEA acted as the chelating agent/complexant [38], whereas ethanol acted as the main solvent. The CZT solution was prepared with Cu/(Zn+Sn) and Zn/Sn ratios of 0.75 and 1.00, respectively, which were the optimal conditions for the growth of high-quality, copper-poor, zinc-rich CZTSe thin films in the final process [39–41]. The CZT film precursor was made from annealed CZT solution precursor prepared with Cu^{2+}, Zn^{2+} and Sn^{4+} metal salts, such as copper (II) acetate monohydrate, zinc acetate dihydrate and tin (IV) chloride dehydrate, purchased from Sigma Aldrich. All metal salts were separately dissolved under ultrasonic assistance in 10 mL of MEA, which was also purchased from Sigma Aldrich. The concentrations of copper, zinc and tin were 0.075, 0.050 and 0.050 M, respectively. After each metal salt was dissolved entirely in MEA, all of the solutions were mixed until their colours turned dark blue. Ethanol was then added at the MEA:ethanol ratio of 30:70. The CZT precursor solution was later deposited through

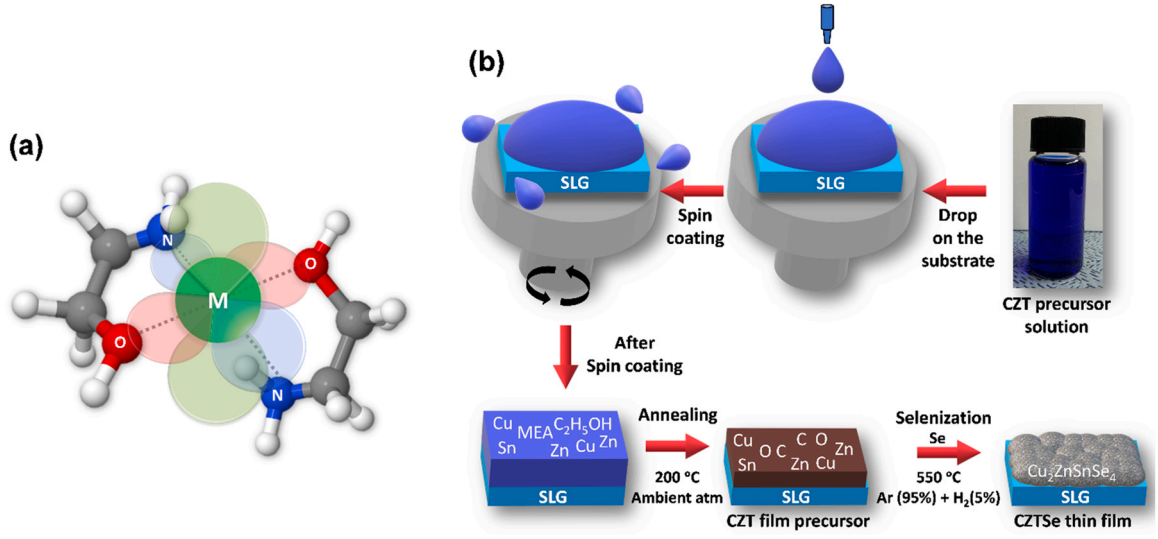

Fig. 1. Schematic of (a) the structure of the metal–MEA complex compound and (b) the synthesis of CZTSe thin films from the CZT precursor.

spin coating at 2000 rpm for 15 s on SLG with dimensions of 2.5 cm × 2.5 cm. Finally, it was annealed under ambient atmosphere at 200 °C for 10 min in a tubular heater until a black-brownish film was obtained.

2.3. Growth of CZTSe thin films

The CZTSe thin films obtained by adding selenium into the CZT precursor through selenization under Ar (95%) and H_2 (5%) mixed gases at 550 °C and a flow rate of 10 sccm for 120 min. After selenization, the sample was cooled to room temperature under natural conditions.

2.4. Characterisation of CZTSe thin films

The microstructural and cross-sectional analyses of the films were performed with a scanning electron microscope by Hitachi (S 4800, Japan) at an operating voltage of 15 kV. The composition of the films was examined by using an EDX apparatus by Horiba, Japan, attached to the SEM apparatus with the acceleration voltage, working distance and emission current of 15 kV, 15 mm and 10 μA, respectively. Crystallinity and structural analyses were performed by using an XRD system by Rigaku (DMAX 2500, Japan) with a fixed angle of 2θ and λ = 1.5405 Å. The measurement conditions were kept at 40 kV, 100 mA and scan speed 2θ with the diffraction angle 2θ between 1° and 65°. The complementary XRD data were obtained with a Renishaw (REO2, U.K.) micro-Raman spectrophotometer at 514.5 nm by using an argon ion C.W. laser. The absorption spectra were recorded by a Varian (Carry 5000, USA) UV–Vis–NIR spectrophotometer over the wavelength range of 300–1500 nm. Electrical properties were determined through taking Hall–Effect measurements with Ecopia (HMS-300, USA) at 0.01 μA. FTIR data were recorded by an apparatus by Perkin Elmer (C86199, USA).

3. Results and discussion

3.1. Fabrication of CZTSe thin films

Fig. 1. Schematic of the structure of the metal–MEA complex compound and the synthesis of CZTSe thin films from the CZT precursor. A detailed schematic of the deposition of CZTSe films from the CZT precursor solution is shown in Fig. 1**(b)**. This schematic illustrates the annealing and salinisation processes. In the preparation process, the CZT precursor solution was deposited onto SLG. In this step, metal–MEA complex compounds were slightly decomposed, and intermetallic atoms produced a binary alloy. By contrast, organic compounds, such as acetate, ethanol and MEA, decomposed partially into organic residues (e.g. C or CO) in the form of amorphous substances that were deposited along with copper and intermetallic binary alloy.

The reactions of copper, zinc and tin in the metal salts with MEA before annealing are given below.

$$M^{x+}\ (aq) + MEA\ (l) \rightarrow M[MEA]_x\ (aq), \quad (1)$$

$$M[MEA]_x\ (aq) \rightarrow M\ (s) + Organic\ residue\ (s), \quad (2)$$

$$Cu\ (s) + Zn\ (s) \rightarrow Cu_xZn_y\ (s), \quad (3)$$

$$Cu\ (s) + Sn\ (s) \rightarrow Cu_xSn_y\ (s), \quad (4)$$

where M = Cu, Zn and Sn.

3.1.1. Structural and surface properties of CZTSe thin films

The resulting XRD pattern of the annealed CZT precursor film is shown in Fig. 2. The pattern contained two diffraction peaks at 2θ = 43.3° and 50.4° that were assigned to the (111) and (200) planes, respectively.

These peaks were likely exhibited by copper and intermetallic binary alloys, e.g. Cu_xZn_y and Cu_xSn_y. The organic amorphous residue surrounding these compounds presented a broad 2θ peak below 35°. The Cu–Zn–Sn ternary phase diagram indicated that both intermetallic compounds may form below 200 °C. However, no evidence for the Zn_xSn_y compound or even metal oxides from the metal–MEA complex compound was found due to the preferential reaction of zinc and tin with copper. The initial chemical composition of the CZT precursor was also similar to the result published by Wibowo et al. [42]. In this study, the chemical compositions of copper, zinc and tin were maintained at 45%, 30% and 25%, respectively, with the Cu/(Zn+Sn) ratio of 0.82 matching the XRD pattern with the Cu–Zn–Sn ternary phase diagram shown in Fig. 2**(a)**. In addition to inorganic compounds, organic compounds, such as acetate from metal salts, ethanol and MEA, were used as solvents in this work. These compounds could leave organic residues in the film in the form of carbon or graphite. FTIR and Raman measurements would help trace such organic residues. The resultant FTIR and Raman spectra of the CZT precursor before and after annealing are presented in Fig. 2**(b)** and **(c)**, respectively. In Fig. 2**(b)**, the peaks at 1365 and 1469 cm^{-1} could be attributed to ethanolic CH_2 and CH_3 group peaks. A peak at 1469 cm^{-1} arising from the CH_2 group in MEA was found in addition to the peak for the CH_3 group in ethanol. The broad peak at 3353 cm^{-1} originated from hydroxyl influenced by hydrogen bonding from the solvent. The peaks at 3287, 1078, 1032 and 1592 cm^{-1} belonged to N–H and were specific indications of the aliphatic amine group. The peaks at 2932 and 2869 cm^{-1} confirmed hydrocarbon (C–H) bonding. Overall, the spectrum of CZT precursors in the solution phase was dominated by the spectrum of MEA because ethanol is molecularly similar to MEA. Therefore, the ethanol peaks were covered by the MEA peaks. The spectrum of the CZT precursor after annealing was different from that of the CZT precursor in the solution phase and could be shifted, show decreased intensity or even disappear. These differences provided evidence for the partial decomposition of organic compounds in the CZT precursor. However, MEA had amine and hydroxyl as active sites. Both sites could react with some compounds during calcination. This reaction can be identified as the broad peak at 3422 cm^{-1} which could be attributed to the hydroxyl site (–OH) from an ester lacking hydrogen bonding between the ligand and the solvent. The peak at 2215 cm^{-1} specifically represented the nitrile group, and the peaks at 2932 and 2869 cm^{-1} represented C–H bonding that remained even after annealing.

The shoulder peaks at 1700 and 1627 cm^{-1} reflected C=O bonding and the −N − H group, respectively. The condition of the CZT precursor after calcination was sufficient to prevent oxidation in the CZT film precursor due to oxidation in the ligand. The XRD pattern of the CZT precursors selenized at elevated temperatures is shown in Fig. 3**(a)**. During selenization at 250 °C, the CZT precursor was reacted with selenium. Selenium had already evaporated at small amounts to form SnSe, which exhibited a peak at 2θ = 31.37°. CuSe, which presented a small peak at 2θ = 25.63°, was also likely present. In addition to CuSe and SnSe, Cu_xZn_y and Cu_xSn_y binary alloys formed under the above condition given that they were the dominant compounds at this moment. At 350 °C, binary and ternary compounds were present along with quaternary compounds. The binary compounds included CuSe, Cu_2-Se_x and SnSe. The ternary and quaternary compounds $CuSnSe_3$ and CZTSe also formed. At 450 °C and 550 °C, five peaks that can be indexed to (101), (112), (211), (204/220) and (312/116) were found at 2θ = 17.35°, 27.13°, 36.11°, 45.09° and 53.45°, respectively. These peaks were indexed to Cu_2SnSe_3 (ICDD: 01-089-1879) or CZTSe (ICDD: 00-052-0868). Moreover, the formation of the CZTSe thin film was confirmed by the Raman spectra given in Fig. 3**(b)**.

The reactions of the CZT precursor could be divided into primary, binary, ternary and quaternary reactions to understand their

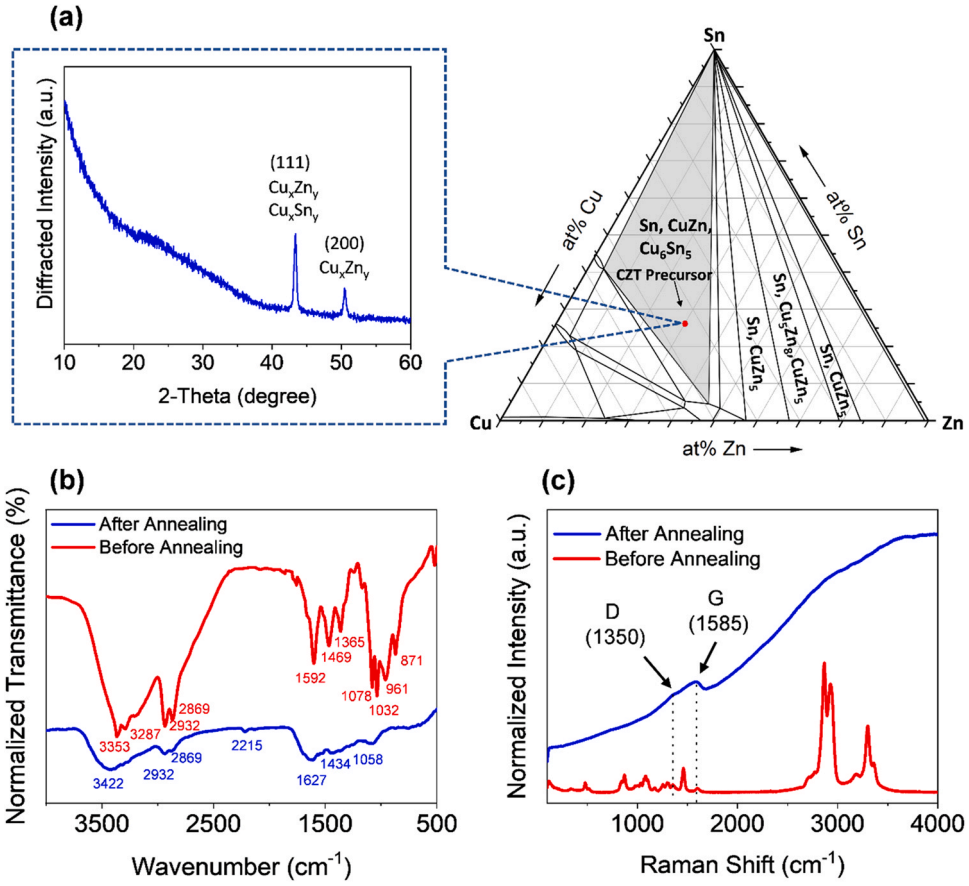

Fig. 2. (a) XRD pattern of the annealed CZT precursor with a particular composition in the Cu–Zn–Sn ternary phase diagram. (b) FTIR spectrum and (c) Raman spectrum of the CZT precursor before and after annealing.

mechanisms. The primary reaction occurred between Se and H_2 and amongst copper, zinc and tin. It produced binary compounds, such as H_2Se, Cu_xSe, ZnSe and SnSe. The binary reaction took place because some binary compounds, such as Cu_xSe, ZnSe, SnSe, CuZn and CuSn, reacted with H_2Se to form the ternary compound Cu_2SnSe_3. The reaction of the ternary compound Cu_2SnSe_3 with ZnSe led to the quaternary reaction. All these reactions are provided below.

Primary reactions:

$$Se\ (g) + H_2\ (g) \rightarrow H_2Se\ (g), \quad (5)$$

$$Cu\ (s) + H_2Se\ (g) \rightarrow Cu_xSe\ (s) + H_2\ (g), \quad (6)$$

$$Zn\ (s) + H_2Se\ (g) \rightarrow ZnSe\ (s) + H_2\ (g), \quad (7)$$

$$Sn\ (s) + H_2Se\ (g) \rightarrow SnSe\ (s) + H_2\ (g), \quad (8)$$

$$C\ (s) + 2\,H_2\ (g) \rightarrow CH_4\ (g). \quad (9)$$

Binary reactions:

$$CO\ (s) + 2\,H_2\ (g) \rightarrow CH_4\ (g) + H_2O\ (g), \quad (10)$$

$$CuZn\ (s) + H_2Se\ (g) \rightarrow Cu_xSe\ (s) + ZnSe\ (s) + H_2\ (g), \quad (11)$$

$$CuSn\ (s) + H_2Se\ (g) \rightarrow Cu_xSe\ (s) + SnSe\ (s) + H_2\ (g). \quad (12)$$

Tertiary reactions:

$$CuSe\ (s) + CuSn\ (s) + 2\,H_2Se\ (g) \rightarrow Cu_2SnSe_3\ (s) + 2\,H_2\ (g), \quad (13)$$

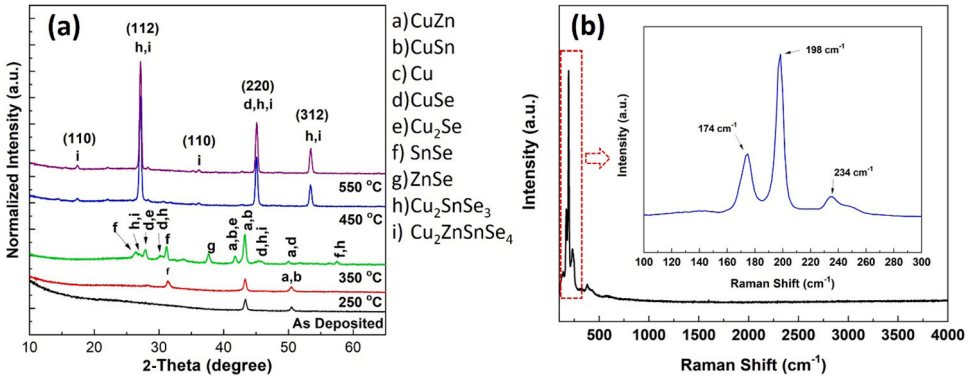

Fig. 3. (a) XRD pattern of the CZT precursors selenized at high temperatures under Ar (95%) + H_2 (5%) for 120 min (c) Raman spectrum of the CZTSe thin film. The inset shows an expanded view of the Raman shift from 100 cm^{-1} to 300 cm^{-1}.

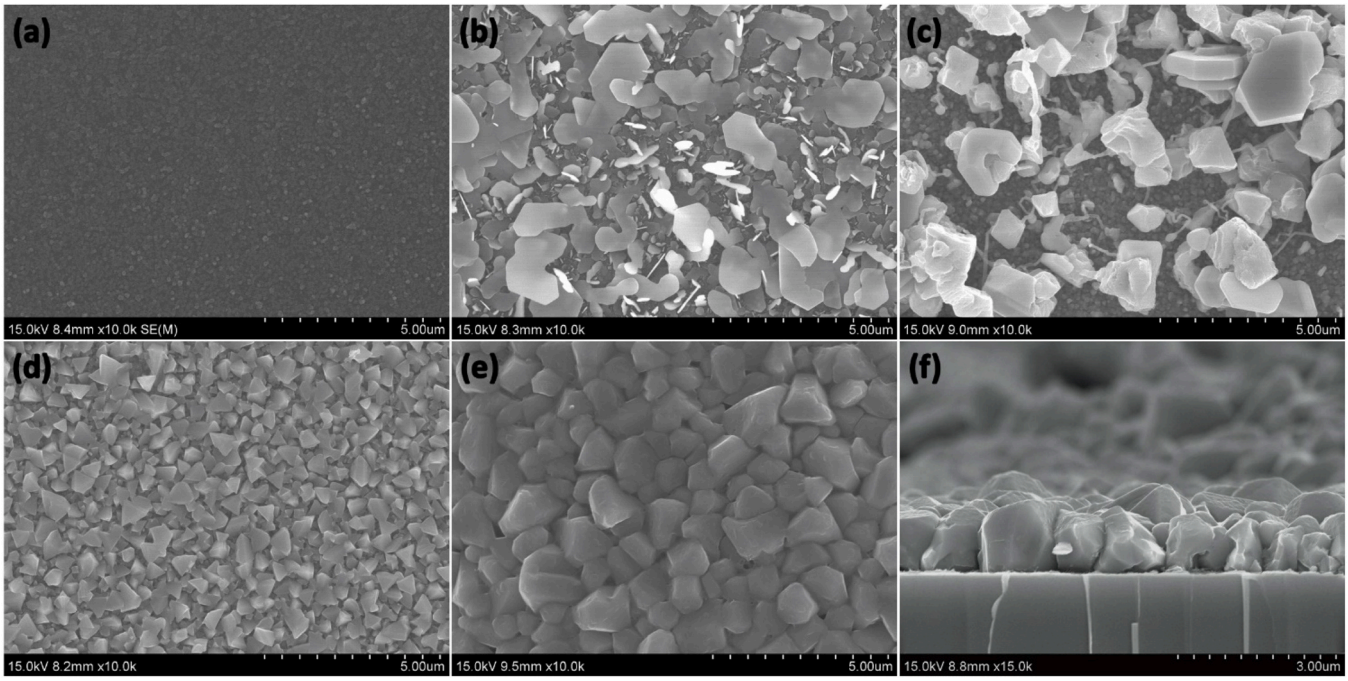

Fig. 4. SEM images of (a) the CZT precursor; (b) the CZT precursor during selenization at 250 °C, (c) 350 °C, (d) 450 °C and (e) 550 °C under Ar (95%) + H_2 (5%) atmosphere for 120 min and (f) the cross-section of the CZT precursor.

$$Cu_2Se\ (s) + SnSe\ (s) + H_2Se\ (g) \rightarrow Cu_2SnSe_3\ (s) + H_2\ (g), \quad (14)$$

$$CuSn\ (s) + H_2Se\ (g) \rightarrow Cu_2SnSe_3\ (s) + H_2\ (g)\cdot \quad (15)$$

Quaternary reaction:

$$Cu_2SnSe_3\ (s) + ZnSe\ (s) \rightarrow Cu_2ZnSnSe_4\ (s)\cdot \quad (16)$$

The Raman spectra confirmed that the CZTSe thin film had formed. The alteration of the selenization temperature from 250 °C to 550 °C led to the presence of carbon in the films. Initially, no peak was observed in the CZT precursor. However, at 250 °C, the peak at 258 cm^{-1} is represents to CuSe or Cu_2Se compounds. In addition, the reaction products between copper in the CZT precursor and selenium during selenization at 350 ºC also appears at 258 cm^{-1}. At 450 °C, the CZTSe peak appeared at 198 cm^{-1}. The Raman spectra also indicated that organic residue existed in the carbon compounds in the form of amorphous carbon. A spectrum with a slope and the specific pattern of D and G peaks at 1350 and 1585 cm^{-1}, respectively, was obtained. The D and G peaks in the Raman spectra disappeared gradually with the increase in temperature. Finally, at 550 °C, the Raman spectra revealed specific peaks for CZTSe at 174, 198 and 234 cm^{-1} and no D and G peaks as shown in Fig. 3**(b)**. The Raman spectra for CZTSe with the confirmation peaks and carbon residue are shown in Fig. S1 and S2, respectively.

The surface and cross-sectional morphologies of the CZT precursor film are provided in Fig. 4**(a)**. The precursor film exhibited a small grain. As shown in Fig. 4**(b),** the SEM image shows hexagonal shape indicated the presence of the CuSe (Cu_2-Se_x) compound and the formation of a small amount of SnSe in the film selenized at 250 °C. In the film selenized at 350 °C, the Se binary compounds CuSe, ZnSe and SnSe were observed with hexagonal, tetragonal and thread-like shapes, respectively, as depicted in Fig. 4**(c)**. The SEM images were consistent with the previously studied XRD patterns and Raman spectra. The film selenized at 450 °C exhibited a small CZTSe grain size as illustrated in Fig. 4**(d)**. Nevertheless, grain size greatly increased at elevated temperatures (550 °C), resulting in the formation of CZTSe films with high crystallinity as presented in Fig. 4**(e)**. In the film selenized at 550 °C, CZTSe had a granular and compact shape with a thickness of approximately 1300 nm as depicted in Fig. 4**(f)**. This result was also consistent with the Raman spectrum results for the films selenized at the elevated temperatures of 450 °C and 550 °C.

The chemical compositions of CZTSe films prepared at different selenization temperatures were determined by using EDX. At elevated temperatures, the amount of selenium increased due to the presence of compounds containing selenium, including primary, binary, tertiary and quaternary compounds. In addition, the evaporation of some elements (e.g. tin) during selenization led to a change in the films' chemical composition. Fig. S3 and Table S1 in the Supporting Information present the change in chemical composition with the variation in selenization temperatures. Chemical composition was determined by comparing the intensity of each element in the sample. For example, if the amount of selenium in the sample had increased, that of the other components should decrease. Hence, the chemical composition ratio was considered in the current study. We used the component ratio (Cu/[Zn+Sn], Zn/Sn and Se/metal) approach to describe the chemical composition of the thin films. This information would help identify the change in the tin and selenium contents in the film. Thus, the Cu/Zn and Cu/Sn ratios should be calculated to describe the change in copper and zinc contents during selenization.

3.1.2. Optoelectronic properties of CZTSe thin films

Chemical composition greatly influences the optoelectronic properties of films. The transmission and absorption of the deposited thin films were determined via UV–vis measurements, which enabled the further calculation of the absorption coefficient and bandgap of the films. Fig. 5**(a)** and **(b)** exhibit the absorbance and wavelength-dependent transmittance of the films fabricated at different selenization temperatures. The fabricated thin films showed high absorption up to 900 nm wavelength and were thus suitable for photovoltaic applications. At wavelengths over 900 nm, the CZTSe thin films presented considerable transmission (~80%) with negligible absorption.

Fig. 5**(c)** illustrates that the absorption coefficient of the films exceeded 10^4 cm^{-1} [43]. The images of the CZT precursor before and

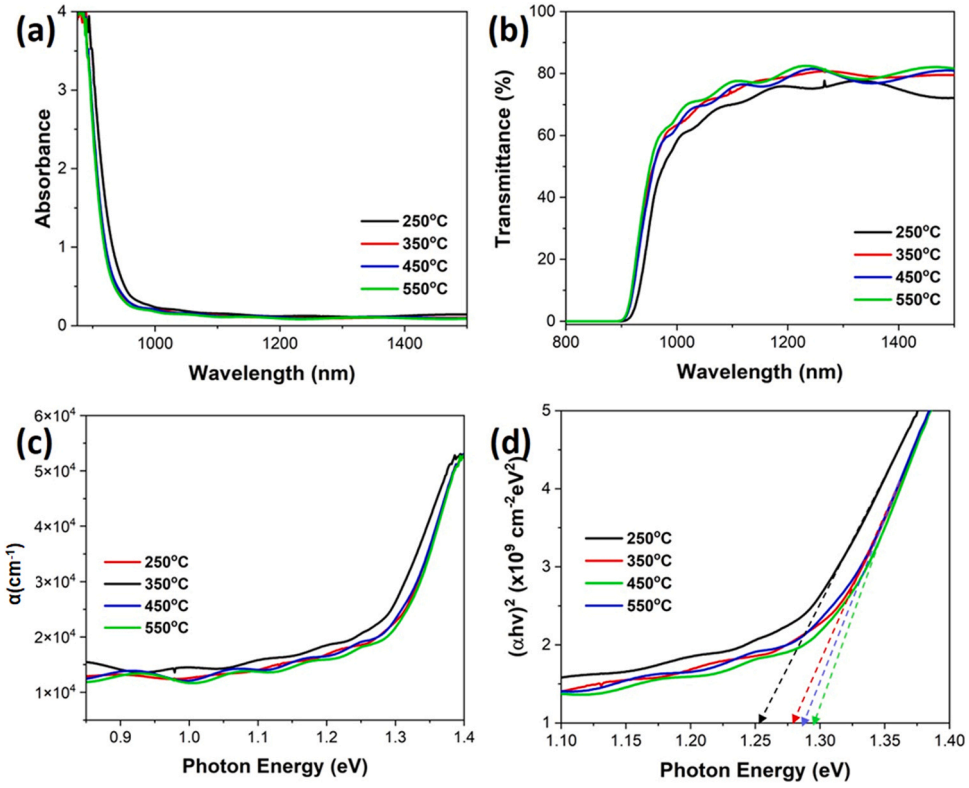

Fig. 5. (a) Absorbance, (b) transmittance, (c) absorption coefficient and (d) Tauc plot for determining the direct optical bandgap of CZTSe films. The films were annealed at 250 °C to 550 °C for 120 min under Ar (95%) + H_2 (95%) atmosphere.

after selenization are provided in Fig. S4**.** The infrequency of optical phenomena in the CZTSe films confirmed the effectiveness of film deposition and the potential for fabricating CZTSe solar cells with high efficiency. Fig. 5**(d)** shows the Tauc plot for the determination of bandgaps with the variation in selenization temperature. The bandgaps of the CZTSe films fabricated at the selenization temperatures of 250 °C, 350 °C, 450 °C and 550 °C were 1.25, 1.27, 1.28 and 1.29 eV, respectively. These bandgaps are very suitable for obtaining efficient CZTSe solar cells. The electrical properties, such as carrier concentration, carrier mobility, conductivity and resistivity, of the deposited CZTSe thin films were determined by using Hall measurements. The electrical properties of the films were found to be influenced mainly by the organic and inorganic phases of the films.

The electrical properties of the films gradually changed as the selenization temperature was increased from 250 °C to 550 °C. The thin film fabricated at the selenization temperature of 250 °C was dominated by organic residues and still had a low content of metal selenide compounds. CZTSe had low carrier concentration and mobility and manifested high resistivity because it contained carbon residue that acted as an insulator. Furthermore, at elevated selenization temperatures, carrier concentration and mobility gradually increased, whereas resistivity gradually decreased because binary and ternary compounds started to form and carbon residues slowly disappeared at 350–450 °C. Finally, at 550 °C, CZTSe developed without any secondary and ternary phases. The measured carrier concentration, mobility and resistivity of the CZTSe thin films selenized at high temperatures are shown in Table 1.

3.2. Examination of the optoelectrical properties of CZTSe thin films via device modelling

The absorbing material is crucial for solar cells because it absorbs sunlight and transports the resulting charge carriers to electrical

Table 1
Electrical properties of the CZT precursor selenized at elevated temperatures under Ar (95%) + H_2 (5%) for 120 min.

Temp (°C)	Carrier Concentration (cm^3)	Mobility (cm^2/Vs)	Resistivity (Ω-cm)
250	1.72×10^{11}	1.28×10^{-6}	2.55×10^{1}
350	5.70×10^{15}	4.30×10^{-5}	3.25×10^{0}
450	8.26×10^{17}	1.05×10^{0}	3.40×10^{-2}
550	1.75×10^{18}	3.20×10^{0}	6.48×10^{-2}

contacts. CZTS, CZTSe, perovskite and CIGS are considered to be the most promising photovoltaic absorber materials [44–46]. The investigated CZTSe thin films exhibited excellent optoelectronic properties suitable for obtaining efficient solar cells. The experimental findings for the fabricated CZTSe thin films were comparable with the best results reported in the literature [42,47].

We designed and modelled a CZTSe solar cell on the basis of the experimental properties in this study. Then, we investigated the photovoltaic properties of the proposed CZTSe solar cells and compared them with the values reported in the literature. In the first step, we utilised SCAPS-1D to study planar CZTSe solar cells [48–50]. SCAPS characterises the parameters of solar cell performance in one dimension. Given that we addressed only the planar structure, we can provide reasonable estimations while considering possible assumptions. The simulation provides the current–voltage (J–V) characteristics of solar cells. Photovoltaic performance parameters can then be extracted. Additional details of the SCAPS-1D electrical simulation method are provided in **Section S1** of the Supporting Information. In this method, experimentally obtained electronic parameter values were used as inputs. Fig. 6**(a)** depicts the schematic of the investigated CZTSe solar cell. The material properties that were input in the simulation are given in Tables 2, 3 and 4. A substrate-type configuration was considered in the design of the solar cell. The CZTSe absorber was placed on top of a thick Mo-

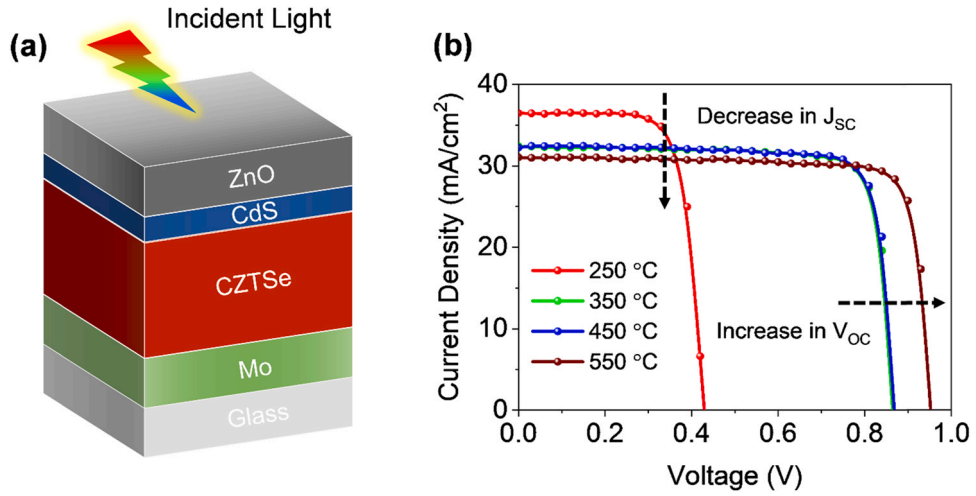

Fig. 6. (a) Schematic of the studied CZTSe solar cell. (b) Comparison of the current–voltage characteristics of CZTSe solar cells prepared with CZTSe thin films fabricated at different selenization temperatures.

Table 2
Material properties used for simulations.

Parameters	*ZnO* [51]	*CZTSe* [52,53]	*CdS* [54]
Thickness (nm)	80	1500	100
E_g *(eV)*	3.3	Experiment (1.25–1.29 eV)	2.4
χ *(eV)*	4.4	4.55–4.49	4.2
ε_r	9	9.4	10
Nc (cm^{-3})	2.5×10^{18}	2.2×10^{18}	2.2×10^{18}
Nv (cm^{-3})	2.0×10^{19}	1.5×10^{19}	1.8×10^{19}
μ_e (cm^2/Vs)	100	100	100
μ_h (cm^2/Vs)	25	12.5	25
N_D (cm^{-3})	1.0×10^{18}	–	1.5×10^{17}
N_A (cm^{-3})	–	Experiment	–

Table 3
Device parameters used in the simulation.

Simulated cell properties	
Cell temperature	300 K
Series resistance R_s	4.25 Ωcm^2
Shunt resistance R_{sh}	370 Ωcm^2

coated glass substrate, followed by 100 nm CdS and 80 nm ZnO layers, where the incident light hit the ZnO layer first then propagated to the bulk of the device.

The simulated J–V curves provided in Fig. 6(**b**) revealed that the J_{SC} of the solar cell gradually decreased with the increase in the temperature. By contrast, the V_{OC} of the solar cell had increased. Evidently, the annealing temperature of the CZTSe film not only influenced the film properties but also affected the optoelectronic properties of the CZTSe solar cells. V_{OC} increased due to two factors: the change in bandgap and carrier concentration. The bandgap of CZTSe increased with the annealing temperature because of the increase in V_{OC} and the decrease in J_{SC}. V_{OC} had a significant relationship with carrier concertation. This relationship is expressed by Eq. (17).

$$v_{oc} = \frac{kT}{q} ln\left[\frac{(N_A + \Delta n)\Delta n}{n_i^2}\right], \tag{17}$$

where kT/q is the thermal voltage, N_A is the donor concentration, Δn is the excess carrier concentration and n_i is the intrinsic carrier concentration. V_{OC} increased with the increase in donor concentration when the other factors were held constant. The experiment demonstrated that CZTSe carrier concentration had increased with the elevation of annealing temperature. This increment also contributed to the increase in the V_{OC} of the device. The J_{SC} and V_{OC} varied from 36.5 mA/cm^2 to 31.5 mA/cm^2 and from 0.42 V to 0.95 V, respectively, when the annealing temperature of the CZTSe film was varied from 250–550 °C. Hence, optimisation was required to maintain the trade-off between photovoltaic parameters. The temperature-dependent J_{SC}s and V_{OC}s of the simulated CZTSe solar cells are presented in Fig. S5 along with the bandgaps of the annealed CZTSe thin films. The CZTSe film had to be annealed at approximately 360 °C to achieve the optimal point. At the optimal point, the V_{OC} and J_{SC} were approximately 0.75 V and 34.5 mA/cm^2, respectively, with a fill factor (FF) of ~82%. The theoretical CZTSe bandgap of the optimised solar cell was assumed to be within the range of 1.25–1.27 eV and can absorb photons at up to 980–992 nm incident wavelength. Therefore, the estimated PCE of the optimised CZTSe solar cell could reach 21.4%.

One-dimensional (1D) numerical simulations cannot provide a complete understanding of the underlying device optics. Solar cell optics has a great influence on solar cell efficiency. 1D and three-dimensional (3D) simulations are exceptionally valuable for device characterisation before proceeding to real fabrication, which is costly and time-consuming. However, a trade-off between 1D and 3D simulations always exists and must be properly maintained. 1D simulation shows the entire system design and the interactions of

Table 4
Contact material properties used in the simulation.

Contact material properties			
Property	Front contact	Back contact	
Surface recombination velocity of electrons	10^7 cm/s	10^5 cm/s	10^5 cm/s
Surface recombination velocity of holes	10^5 cm/s	10^7 cm/s	10^7 cm/s
Metal work function	Flat band	Flat band	Mo (5 eV)

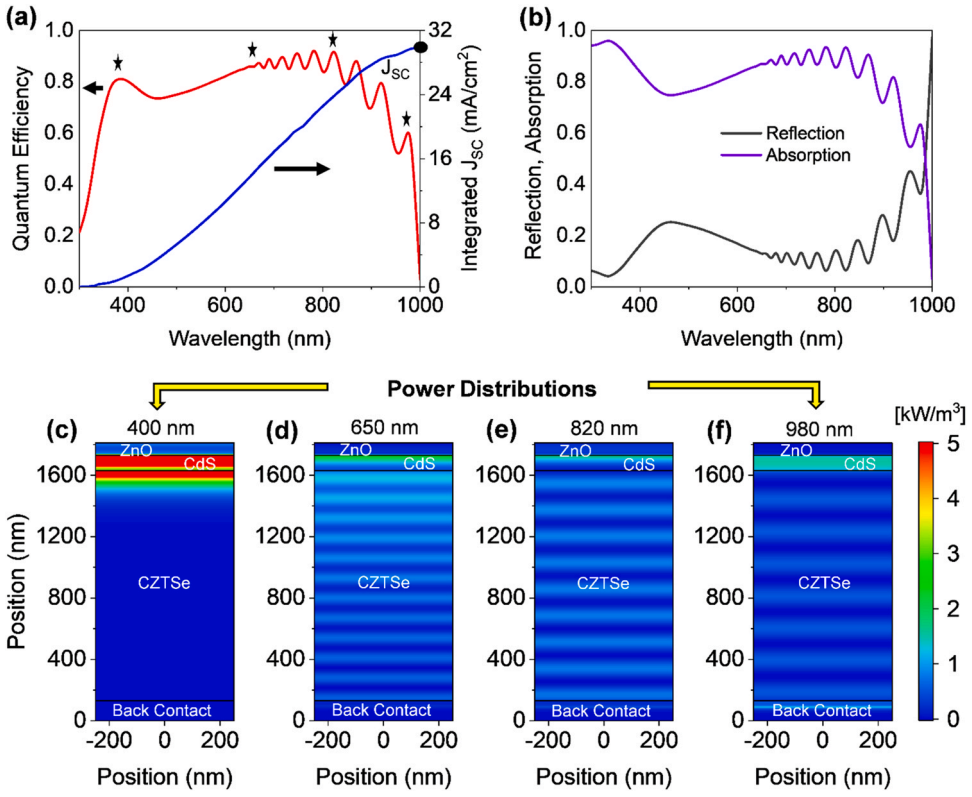

Fig. 7. Simulated (a) QE and integrated J_{SC}, (b) absorption and reflection of the CZTSe solar cell. Cross-sectional power density maps of the investigated solar cell under monochromatic illumination of (c) 400 nm, (d) 650 nm, (e) 820 nm and (f) 980 nm.

different components within a system. In other words, 1D simulation calculates the field in one direction (X or Y plane) by using analytical equations. Hence, 1D simulation is beneficial for optimising systems and determining the theoretical upper limit of device efficiency, which is higher than experimental outcomes. By contrast, the 3D simulation is appropriate for identifying the optimal design characteristics of individual components because it considers every aspect within systems. A 3D solver computes an electric field in all directions (X, Y and Z planes) by discretising the cell into extremely small blocks (a mesh). The size of an individual mesh is only a few nanometres. Therefore, 3D simulations require higher computational efforts (memory and time) than 1D simulations. Fig. S6 provides an overview of the different environments of the simulation. The findings of 3D simulations are in excellent agreement with the experimental results as confirmed in our previously published works [4,36]. Investigating the optical wave phenomena within a solar cell structure in three dimensions is essential to determine realistic photovoltaic performance [55–57]. Hence, as a second step, 3D FDTD optical simulations were carried out to study the electromagnetic wave propagation and optical characteristics of solar cells [36,58–60]. The optimised device structure was considered for the optical simulation, wherein complex refractive indices derived from the optical investigation of materials were used as input parameters. The optical wave propagation for the device was modelled over the wavelength range of 300–1000 nm, which was close to the fabricated CZTSe absorber bandgap (~1.25 eV). The incident plane wave was circularly polarised with an amplitude of 1 V/m. The FDTD simulation results for the electromagnetic field distribution within the solar cell further enabled the calculation of the power density, quantum efficiency (QE) and J_{SC} of the solar cell [37]. A detailed discussion of power density, QE and J_{SC} calculation is provided in the Supporting Information (**Section S2**). The maximum value of the collection efficiency is expected to be unity. Fig. 7**(a)** shows the calculated QE and corresponding integrated J_{SC} of the investigated CZTSe solar cell. The QE exhibited large variation throughout the whole spectrum, and photons were absorbed up to 1000 nm, which well matched the theoretical estimation based on the obtained CZTSe bandgap. However, the calculated J_{SC} of the solar cell was 30 mA/cm^2, which was almost 4.5 mA/cm^2 lower than the J_{SC} estimated by the 1D simulation. Nevertheless, such a discrepancy is acceptable for this study given that the optical simulation considered a 3D environment. Compared with that in short wavelengths, QE in long wavelengths exhibited a higher number of interference fringes due to several forward and backward wave propagations in the extended wavelength region. These optical phenomena can be further confirmed by the simulated power density profiles for the incident wavelengths of 400, 650, 820 and 980 nm shown in Fig. 7**(c–f)**.

CZTSe had a high absorption coefficient at short wavelengths. Hence, photon absorption was considerably higher in the short wavelength region than in the longer wavelength region. However, as shown in Fig. 7**(d)**, in short wavelengths (< 400 nm), most incident photons were either absorbed through contact with the buffer layers or the CdS/ CZTSe interface, where photons travelled by a few hundred nanometres to the CZTSe layer. Such optical phenomena occurred due to the optical properties of the contact and buffer materials. Fig. S7 in the Supporting Information shows the complex refractive index (refractive index *n* and extinction coefficient k) of CdS and ZnO. Both materials were clearly demonstrated to have high absorption coefficients ($\alpha = 4\pi k/\lambda$) for wavelengths below 400 nm. Beyond 400 nm, the extinction coefficient of ZnO was almost zero, whereas that of CdS was reduced to less 50%, which greatly influenced photon absorption (QE) in the solar cell.

With the increase in wavelength (650 nm), the absorption in the absorber layer increased as also shown in Fig. 7**(e)**. However, a further increase in wavelengths (Fig. 7**[e]**) led to a limit on the QE due to several constructive and destructive interferences. At 980 nm, photon absorption in the device was almost zero due to the material

Table 5
Comparison of the photovoltaic performances of the CZTSe solar cells.

Cell Structure	*V_{OC} (V)*	*J_{SC} ($mAcm^{-2}$)*	*FF (%)*	*PCE (%)*	*Year*	*Ref.*
CZTSe/CdS	0.513	35.2	69.8	12.6	2014	[61]
CZTSe/CdS	0.41	37.27	73.79	11.43	2019	[62]
CZTSe/CdS	0.38	35.36	59.9	8.2	2016	[63]
Mo/CZTS-Ti/CdS	0.77	21.0	61	14.1	2018	[64]
Mo/CZTS/CdS	0.88	28.5	66	16.9	2018	[65]
CZTSe/CdS	0.75	30	82	**18.5**	2021	This study

properties of the deposited CZTSe film close to the bandgap; nonetheless, a fraction of photons was considered lost due to the plasmonic effects at the metal/semiconductor interface as illustrated in Fig. 7**(f)**. The investigated solar cell's electrical field distribution profiles are provided in Fig. S8 in the Supporting Information. These profiles can further validate the occurrence of optical wave propagation in the device. The investigated solar cells exhibited high reflections because their planar front surface restricted the total photon absorption of the solar cells and did not contribute to the QE, J_{SC} and PCE as shown in Fig. 7**(b)**. Photon absorption can be improved by texturizing the surface or interfaces of solar cells; however, this topic is beyond the scope of the present study [66–68]. We limited our study to the optoelectronic characteristics of a basic CZTSe solar cell to realise our fabricated thin film's potential as an absorber. The CZTSe solar cell had an estimated realistic PCE of ~18.5% and could exhibit a J_{SC} of 30 mA/cm^2, V_{OC} of 0.75 V and FF of 82%. We compared the solar performance of our investigated CZTSe with that of recently published best CZTSe solar cells, which are listed in Table 5, to provide further context. Our findings revealed that the proposed CZTSe solar cell can outperform all similar characterised CZTSe solar cells and advance the realisation of highly efficient CZTSe-based photovoltaic devices.

4. Conclusions

CZTSe thin film was prepared via a two-step reaction method from the CZT precursor and then deposited from the metal–MEA complex compound through selenization without hydrazine addition. The deposited film's structural and optoelectronic properties were studied via necessary material characterisations that confirmed its high quality and potential for use as a photovoltaic absorber. The annealing temperature during film deposition had a great influence on the material properties of the thin film. Organic impurities gradually disappeared due to the effect of the elevated temperature and atmosphere. Notably, the composition of the films changed at elevated selenization temperatures. Organic impurities from organic residues gradually disappeared at 450 °C. An increase in selenization temperature led to an increase in the bandgap of the film. The optical and electrical characteristics of the CZTSe-based solar cells were studied via 1D and 3D numerical simulations to confirm the potential of the deposited CZTSe films. The SCAPS-1D simulation tool was used to investigate J–V characteristics, whereas optical characteristics were determined via FDTD optical simulations in 3D. The optimised bandgap of the CZTSe film was 1.25–1.27 eV, which resulted in an estimated PCE of 18.5% with a J_{SC} of 30 mA/cm^2, V_{OC} of 0.75 V and FF of 82%. The proposed CZTSe solar cell can outperform all best solar cells with similar characteristics and provide a breakthrough in CZTSe solar cells with high photovoltaic performance. We also provided a table comparing the photovoltaic performance of the CZTSe in this work with that of the best CZTSe solar cells in the literature. A detailed systematic investigation of the preparation and application in photovoltaic technology of the CZTSe films was discussed in this manuscript.

CRediT authorship contribution statement

Ersan Y. Muslih: Conceptualization, Methodology, Writing – original draft. **Khan Sobayel Bin Rafiq**: Conceptualization, Investigation, Visualization, Software. **Mohammad Ismail Hossain**: Data curation, Visualization, Formal analysis, Software. **Md. Shahiduzzaman**: Resources, Validation, Methodology, Formal analysis. **Mohammad Junaebur Rashid**: Formal analysis, Data curation. **Tasmiat Rahman**: Validation, Formal analysis, Data curation. **Badrul Munir**: Formal analysis, Data curation. **Khaled Althubeiti**: Data curation, Resources, Writing – review & editing. **Hend I. Alkhammash**: Resources, Data curation, Writing – review & editing. **Huda Abdullah**: Funding acquisition, Writing – review & editing. **K. Techato**: Validation, Writing – review & editing. **Md. Akhtaruzzaman**: Validation, Project administration, Funding acquisition, Supervision, Resources, Writing – review & editing. **Kim Kyoo Ho**: Resources, Project administration, Supervision, Writing – review & editing.

Competing interests

The authors declare no competing interests.

Acknowledgments

This paper is dedicated to Prof. Kim Kyoo Ho, the author's supervisor (Ersan) in Yeungnam University, as his last paper before retirement in appreciation of his kindness. This study was supported by the Basic Science Research Program (2013R1A1A2013408) and Centre for Inorganic Photovoltaic Materials (No. 2012-0001170) through the National Research Foundation of Korea funded by the Ministry of Science, ICT and Future Planning. The authors also extend their appreciation to The University Researchers Supporting Project Number (TURSP-2020/241), Taif University, Taif, Saudi Arabia. The authors also thank the Ministry of Education and Culture of the Republic of Indonesia and all of their collaborators from the University of Indonesia and Kanazawa University. Moreover, the authors thank The National University of Malaysia for the research grant support with code the FRGS/1/2019/STG07/UKM/02/11. The authors gratefully acknowledge Dr. Marc 394 Bargeman, University of Gent, Belgium, for providing the SCAPS simulation software.

Appendix A. Supporting information

Supplementary data associated with this article can be found in the online version at doi:10.1016/j.jallcom.2021.163457.

References

[1] NREL Transforming Energy, Best Research-Cell Efficiency Chart, 2021. https://www.nrel.gov/pv/cell-efficiency.html. (Accessed 2 December 2021).
[2] M.A. Green, E.D. Dunlop, J. Hohl-Ebinger, M. Yoshita, N. Kopidakis, X. Hao, Solar cell efficiency tables (version 56), Prog. Photovolt. Res. Appl. 28 (2020) 629–638, https://doi.org/10.1002/pip.3303
[3] S. Mahesh, J.M. Ball, R.D.J. Oliver, D.P. McMeekin, P.K. Nayak, M.B. Johnston, H.J. Snaith, Revealing the origin of voltage loss in mixed-halide perovskite solar cells, Energy Environ. Sci. 13 (2020) 258–267, https://doi.org/10.1039/c9ee02162k
[4] M.I. Hossain, M. Shahiduzzaman, S. Ahmed, M.R. Huqe, W. Qarony, A.M. Saleque, M. Akhtaruzzaman, D. Knipp, Y.H. Tsang, T. Taima, J.A. Zapien, Near field control for enhanced photovoltaic performance and photostability in perovskite solar cells, Nano Energy 89 (2021) 106388, https://doi.org/10.1016/j.nanoen.2021.106388
[5] C. Yan, J. Huang, K. Sun, S. Johnston, Y. Zhang, H. Sun, A. Pu, M. He, F. Liu, K. Eder, L. Yang, J.M. Cairney, N.J. Ekins-Daukes, Z. Hameiri, J.A. Stride, S. Chen, M.A. Green, X. Hao, Cu2ZnSnS4 solar cells with over 10% power conversion efficiency enabled by heterojunction heat treatment, Nat. Energy 3 (2018) 764–772, https://doi.org/10.1038/s41560-018-0206-0
[6] Z. Zhang, Q. Gao, J. Guo, Y. Zhang, Y. Han, J. Ao, M.J. Jeng, F. Liu, W. Liu, Y. Zhang, Over 10% efficient pure CZTSe solar cell fabricated by electrodeposition with Ge doping, Sol. RRL 4 (2020) 1–9, https://doi.org/10.1002/solr.202000059

[7] W. Wang, M.T. Winkler, O. Gunawan, T. Gokmen, T.K. Todorov, Y. Zhu, D.B. Mitzi, Device characteristics of CZTSSe thin film solar cells with 12.6% efficiency, Adv. Energy Mater. 4 (2014) 1–5, https://doi.org/10.1002/aenm.201301465

[8] O.K. Simya, T. Vijayaraghavan, B. Subramanian, A.M. Ashok, Effect of RF sputter power on deposition of CZTX (X[dbnd]S, Se) active layer without selenization/ sulfurization, for solar cell applications, J. Alloy. Compd. (2021) 162838, https://doi.org/10.1016/j.jallcom.2021.162838

[9] P.K. Nayak, S. Mahesh, H.J. Snaith, D. Cahen, Photovoltaic solar cell technologies: analysing the state of the art, Nat. Rev. Mater. 4 (2019) 269–285, https://doi.org/10.1038/s41578-019-0097-0

[10] H.S. Nugroho, G. Refantero, N.L.W. Septiani, M. Iqbal, S. Marno, H. Abdullah, E.C. Prima, B.Yuliarto Nugraha, A progress review on the modification of CZTS(e)-based thin film solar cells, J. Ind. Eng. Chem. 105 (2022) 83–110, https://doi.org/10.1016/j.jiec.2021.09.010

[11] J. Park, H. Yoo, V. Karade, K.S. Gour, E. Choi, M. Kim, X. Hao, S.J. Shin, J. Kim, H. Shim, D. Kim, J.H. Kim, J. Yun, J.H. Kim, Investigation of low intensity light performances of kesterite CZTSe, CZTSSe and CZTS thin film solar cells for indoor applications, J. Mater. Chem. A 8 (2020) 14538–14544, https://doi.org/10.1039/d0ta04863a

[12] M. He, C. Yan, J. Li, M.P. Suryawanshi, J. Kim, M.A. Green, X. Hao, Kesterite solar cells: insights into current strategies and challenges, Adv. Sci. 8 (2021) 1–16, https://doi.org/10.1002/advs.202004313

[13] F. Martinho, S. Lopez-Marino, M. Espíndola-Rodríguez, A. Hajijafarassar, F. Stulen, S. Grini, M. Döbeli, M. Gansukh, S. Engberg, E. Stamate, L. Vines, J. Schou, O. Hansen, S. Canulescu, Persistent double-layer formation in kesterite solar cells: a critical review, ACS Appl. Mater. Interfaces 12 (2020) 39405–39424, https://doi.org/10.1021/acsami.0c10068

[14] S. Padhy, R. Mannu, U.P. Singh, Graded bandgap structure of kesterite material using bilayer of CZTS and CZTSe for enhanced performance: a numerical approach, Sol. Energy 216 (2021) 601–609, https://doi.org/10.1016/j.solener.2021.01.057

[15] H. Ferhati, F. Djeffal, L.B. Drissi, A new approach to the modeling and simulation of multi-junction solar cells, Optik 200 (2020) 163452, https://doi.org/10.1016/j.ijleo.2019.163452

[16] H. Ferhati, F. Djeffal, Exceeding 30% efficiency for an environment-friendly tandem solar cell based on earth-abundant Se/CZTS materials, Phys. E Low Dimens. Syst. Nanostruct. 109 (2019) 52–58, https://doi.org/10.1016/j.physe.2019.01.002

[17] Z. Zhang, Q. Gao, J. Guo, Y. Zhang, Y. Han, J. Ao, M.-J. Jeng, F. Liu, W. Liu, Y. Zhang, Over 10% efficient pure CZTSe solar cell fabricated by electrodeposition with Ge doping, Sol. RRL 4 (2020) 2000059, https://doi.org/10.1002/solr.202000059

[18] D.B. Mitzi, O. Gunawan, T.K. Todorov, K. Wang, S. Guha, The path towards a high-performance solution-processed kesterite solar cell, Sol. Energy Mater. Sol. Cells 95 (2011) 1421–1436, https://doi.org/10.1016/j.solmat.2010.11.028

[19] T.K. Todorov, J. Tang, S. Bag, O. Gunawan, T. Gokmen, Y. Zhu, D.B. Mitzi, Beyond 11% effi ciency: characteristics of state-of-the-art $Cu_2ZnSn(S,Se)_4$ Solar Cells, Adv. Energy Mater. 3 (2013) 34–38, https://doi.org/10.1002/aenm.201200348

[20] E.Y. Muslih, K.H. Kim, Characteristics of Cu_2nSnS_4 thin film prepared by calculation and sulfurizing of metal (Cu, Zn, Sn) -ethanolamine precursor complexed from metal (Cu, Zn, Sn) -hydrate, Chalcogenide Lett. 12 (2015) 349–355.

[21] M. Ikhlasul Amal, K.H. Kim, Structural and optical properties of sulfurized Cu_2ZnSnS_4 thin films from Cu–Zn–Sn alloy precursors, J. Mater. Sci. Mater. Electron. 24 (2013) 559–566, https://doi.org/10.1007/s10854-012-0858-7

[22] B. Munir, B.E. Prastyo, E.Y. Muslih, D.M. Nurjaya, Non-sulfurization single solution approach to synthesize CZTS thin films, Int. J. Technol. 7 (2016) 1326–1334, https://doi.org/10.14716/ijtech.v7i8.6887

[23] T. Todorov, M. Kita, J. Carda, P. Escribano, Cu_2ZnSnS_4 films deposited by a soft-chemistry method, Thin Solid Films 517 (2009) 2541–2544, https://doi.org/10.1016/j.tsf.2008.11.035

[24] Y. Sun, Y. Zhang, H. Wang, M. Xie, K. Zong, H. Zheng, Y. Shu, J. Liu, H. Yan, M. Zhu, W. Lau, Novel non-hydrazine solution processing of earth-abundant $Cu_2ZnSn(S,Se)_4$ absorbers for thin film solar cells, J. Mater. Chem. A 1 (2013) 6880–6887, https://doi.org/10.1039/C3TA10566K

[25] E.C. Prima, L.H. Wong, A. Ibrahim, B. Nugraha, Yuliarto, Solution-processed pure Cu_2ZnSnS_4/CdS thin film solar cell with 7.5% efficiency, Opt. Mater. 114 (2021) 110947, https://doi.org/10.1016/j.optmat.2021.110947

[26] Y.E. Romanyuk, C.M. Fella, A.R. Uhl, M. Werner, A.N. Tiwari, T. Schnabel, E. Ahlswede, Recent trends in direct solution coating of kesterite absorber layers in solar cells, Sol. Energy Mater. Sol. Cells 119 (2013) 181–189, https://doi.org/10.1016/j.solmat.2013.06.038

[27] T. Todorov, D.B. Mitzi, Direct liquid coating of chalcopyrite light-absorbing layers for photovoltaic devices, Eur. J. Inorg. Chem. (2010) 17–28, https://doi.org/10.1002/ejic.200900837

[28] E. Peksu, H. Karaagac, Characterization of Cu_2ZnSnS_4 thin films deposited by one-step thermal evaporation for a third generation solar cell, J. Alloy. Compd. 862 (2021) 158503, https://doi.org/10.1016/j.jallcom.2020.158503

[29] B. Roy, S. Bandyopadhyay, The design strategies and mechanisms of fluorogenic and chromogenic probes for the detection of hydrazine, Anal. Methods 10 (2018) 1117–1139.

[30] R.L. Sackheim, R.K. Masse, Green propulsion advancement: challenging the maturity of monopropellant hydrazine, J. Propuls. Power 30 (2014) 265–276.

[31] S. Tripathi, B. Kumar, D.K. Dwivedi, Study on formation and characterization of kesterite CZTSSe thin films deposited by thermal evaporation technique for solar cell applications, J. Mater. Sci. Mater. Electron. 31 (2020) 8308–8315, https://doi.org/10.1007/s10854-020-03366-y

[32] S. Wang, Z. Shen, Y. Sun, H. Li, K. Zhang, L. Wu, J. Ao, Y. Zhang, Defects and surface electrical property transformation induced by elemental interdiffusion at the p–n heterojunction via high-temperature annealing, ACS Appl. Mater. Interfaces 13 (2021) 12211–12220, https://doi.org/10.1021/acsami.1c00096

[33] Y. Altowairqi, A. Alsubaie, K.P. Stroh, I.G. Perez-Marin, L. Bowen, M. Szablewski, D.P. Halliday, The effect of annealing conditions: temperature, time, ramping rate and atmosphere on nanocrystal Cu2ZnSnS4 (CZTS) thin film solar cell properties, Mater. Today Proc. 18 (2019) 473–486. ⟨https://doi.org/10.1016/j.matpr.2019.06.234⟩.

[34] H. Yoo, J.S. Jang, S.W. Shin, J. Lee, J.H. Kim, D.M. Kim, I.J. Lee, B.H. Lee, J. Park, J.H. Kim, Influence of the reaction pathway on the defect formation in a $Cu_2ZnSnSe_4$ thin film, ACS Appl. Mater. Interfaces 13 (2021) 13425–13433, https://doi.org/10.1021/acsami.1c01307

[35] X. Xu, L. Guo, J. Zhou, B. Duan, D. Li, J. Shi, H. Wu, Y. Luo, Q. Meng, Efficient and composition-tolerant kesterite $Cu_2ZnSn(S,Se)_4$ solar cells derived from an in situ formed multifunctional carbon framework, Adv. Energy Mater. 11 (2021) 2102298, https://doi.org/10.1002/aenm.202102298

[36] M. Shahiduzzaman, M.I. Hossain, S. Visal, T. Kaneko, W. Qarony, S. Umezu, K. Tomita, S. Iwamori, D. Knipp, Y.H. Tsang, M. Akhtaruzzaman, J.-M. Nunzi, T. Taima, M. Isomura, Spray pyrolyzed TiO_2 embedded multi-layer front contact design for high-efficiency perovskite solar cells, Nano Micro Lett. 13 (2021) 36, https://doi.org/10.1007/s40820-020-00559-2

[37] M.I. Hossain, A.M. Saleque, S. Ahmed, I. Saidjafarzoda, M. Shahiduzzaman, W. Qarony, D. Knipp, N. Biyikli, Y.H. Tsang, Perovskite/perovskite planar tandem solar cells: a comprehensive guideline for reaching energy conversion efficiency beyond 30%, Nano Energy 79 (2021) 105400, https://doi.org/10.1016/j.nanoen.2020.105400

[38] A. Cho, H. Song, J. Gwak, Y.-J. Eo, J.H. Yun, K. Yoon, S. Ahn, A chelating effect in hybrid inks for non-vacuum-processed $CuInSe_2$ thin films, J. Mater. Chem. A 2 (2014) 5087–5094.

[39] M. Dimitrievska, A. Fairbrother, E. Saucedo, A. Pérez-Rodríguez, V. Izquierdo-Roca, Secondary phase and Cu substitutional defect dynamics in kesterite solar cells: impact on optoelectronic properties, Sol. Energy Mater. Sol. Cells 149 (2016) 304–309.

[40] M.A. Olgar, Y. Atasoy, B.M. Başol, M. Tomakin, G. Aygun, L. Ozyuzer, E. Bacaksız, Influence of Cu composition and reaction temperature on the properties of CZTSe thin films, J. Alloy. Compd. 682 (2016) 610–617.

[41] J. Just, C.M. Sutter-Fella, D. Lützenkirchen-Hecht, R. Frahm, S. Schorr, T. Unold, Secondary phases and their influence on the composition of the kesterite phase in CZTS and CZTSe thin films, Phys. Chem. Chem. Phys. 18 (2016) 15988–15994.

[42] R.A. Wibowo, H. Yoo, A. Hölzing, R. Lechner, S. Jost, J. Palm, M. Gowtham, B. Louis, R. Hock, A study of kesterite $Cu_2ZnSn(Se, S)_4$ formation from sputtered Cu–Zn–Sn metal precursors by rapid thermal processing sulfo-selenization of the metal thin films, Thin Solid Films 535 (2013) 57–61.

[43] K. Benyahia, F. Djeffal, H. Ferhati, A. Benhaya, A. Bendjerad, Y. Djaballah, N. Martin, Microstructured ZnO-ZnS composite for earth-abundant photovoltaics: elaboration, surface analysis and enhanced optical performances, Sol. Energy 218 (2021) 312–319, https://doi.org/10.1016/j.solener.2021.02.057

[44] S. Kundu, T.L. Kelly, In situ studies of the degradation mechanisms of perovskite solar cells, EcoMat 2 (2020), https://doi.org/10.1002/eom2.12025

[45] Y. Luan, F. Wang, J. Zhuang, T. Lin, Y. Wei, N. Chen, Y. Zhang, F. Wang, P. Yu, L. Mao, H. Liu, J. Wang, Dual-function interface engineering for efficient perovskite solar cells, EcoMat 3 (2021), https://doi.org/10.1002/eom2.12092

[46] B. Yang, S. Peng, W.C.H. Choy, Inorganic top electron transport layer for high performance inverted perovskite solar cells, EcoMat 3 (2021), https://doi.org/10.1002/eom2.12127

[47] V. Kumar, A. Dutta, U.P. Singh, Optimization of selenization parameters for fabrication of CZTSe thin film, Superlattices Microstruct. 144 (2020) 106578.

[48] K. Sobayel, M. Akhtaruzzaman, K.S. Rahman, M.T. Ferdaous, Z.A. Al-Mutairi, H.F. Alharbi, N.H. Alharthi, M.R. Karim, S. Hasmady, N. Amin, A comprehensive defect study of tungsten disulfide (WS_2) as electron transport layer in perovskite solar cells by numerical simulation, Results Phys. 12 (2019) 1097–1103.

[49] K. Sobayel, M. Shahinuzzaman, N. Amin, M.R. Karim, M.A. Dar, R. Gul, M.A. Alghoul, K. Sopian, A.K.M. Hasan, M. Akhtaruzzaman, Efficiency enhancement of CIGS solar cell by WS_2 as window layer through numerical modelling tool, Sol. Energy 207 (2020) 479–485.

[50] K. Sobayel, K.S. Rahman, M.R. Karim, M.O. Aijaz, M.A. Dar, M.A. Shar, H. Misran, N. Amin, Numerical modeling on prospective buffer layers for tungsten di-sulfide (WS_2) solar cells by SCAPS-1D, Chalcogenide Lett. 15 (2018) 307–315.

[51] G. Kartopu, B.L. Williams, V. Zardetto, A.K. Gürlek, A.J. Clayton, S. Jones, W.M.M. Kessels, M. Creatore, S.J.C. Irvine, Enhancement of the photocurrent and efficiency of CdTe solar cells suppressing the front contact reflection using a highly-resistive ZnO buffer layer, Sol. Energy Mater. Sol. Cells 191 (2019) 78–82.

[52] M.V. Yakushev, M.A. Sulimov, J. Márquez-Prieto, I. Forbes, J. Krustok, P.R. Edwards, V.D. Zhivulko, O.M. Borodavchenko, A.V. Mudryi, R.W. Martin, Influence of the Cu content on the optical properties of CZTSe thin films, Sol. Energy Mater. Sol. Cells 168 (2017) 69–77.

[53] Y.H. Khattak, F. Baig, H. Toura, S. Beg, B.M. Soucase, CZTSe kesterite as an alternative hole transport layer for $MASnI_3$ perovskite solar cells, J. Electron. Mater. 48 (2019) 5723–5733.

[54] F.T. Munna, V. Selvanathan, K. Sobayel, G. Muhammad, N. Asim, N. Amin, K. Sopian, M. Akhtaruzzaman, Diluted chemical bath deposition of CdZnS as prospective buffer layer in CIGS solar cell, Ceram. Int. 47 (2020) 11003–11009.

[55] M.I. Hossain, A.K.M. Hasan, W. Qarony, M. Shahiduzzaman, M.A. Islam, Y. Ishikawa, Y. Uraoka, N. Amin, D. Knipp, M. Akhtaruzzaman, Y.H. Tsang, Electrical and optical properties of nickel-oxide films for efficient perovskite

solar cells, Small Methods 4 (2020) 2000454, https://doi.org/10.1002/smtd.202000454
[56] M.I. Hossain, W. Qarony, V. Jovanov, Y.H. Tsang, D. Knipp, Nanophotonic design of perovskite/silicon tandem solar cells, J. Mater. Chem. A 6 (2018) 3625–3633, https://doi.org/10.1039/c8ta00628h
[57] M.S. Islam, K. Sobayel, A. Al-Kahtani, M.A. Islam, G. Muhammad, N. Amin, M. Shahiduzzaman, M. Akhtaruzzaman, Defect study and modelling of SnX_3-based perovskite solar cells with SCAPS-1D, Nanomaterials 11 (2021), https://doi.org/10.3390/nano11051218
[58] M.I. Hossain, M. Shahiduzzaman, A.M. Saleque, M.R. Huqe, W. Qarony, S. Ahmed, M. Akhtaruzzaman, D. Knipp, Y.H. Tsang, T. Taima, J.A. Zapien, Improved nanophotonic front contact design for high-performance perovskite single-junction and perovskite/perovskite tandem solar cells, Sol. RRL 5 (2021) 2100509, https://doi.org/10.1002/solr.202100509
[59] M. Shahiduzzaman, M. Ismail Hossain, S. Otani, L. Wang, S. Umezu, T. Kaneko, S. Iwamori, K. Tomita, Y. Hong Tsang, M. Akhtaruzzaman, D. Knipp, J.-M. Nunzi, M. Isomura, J. Antonio Zapien, T. Taima, Low-temperature treated anatase TiO_2 nanophotonic-structured contact design for efficient triple-cation perovskite solar cells, Chem. Eng. J. 426 (2021) 131831, https://doi.org/10.1016/j.cej.2021.131831
[60] W. Qarony, M.I. Hossain, V. Jovanov, A. Salleo, D. Knipp, Y.H. Tsang, Influence of perovskite interface morphology on the photon management in perovskite/silicon tandem solar cells, ACS Appl. Mater. Interfaces 12 (2020) 15080–15086, https://doi.org/10.1021/acsami.9b21985
[61] W. Wang, M.T. Winkler, O. Gunawan, T. Gokmen, T.K. Todorov, Y. Zhu, D.B. Mitzi, Device characteristics of CZTSSe thin-film solar cells with 12.6% efficiency, Adv. Energy Mater. 4 (2014) 1301465.
[62] X. Li, D. Zhuang, N. Zhang, M. Zhao, X. Yu, P. Liu, Y. Wei, G. Ren, Achieving 11.95% efficient $Cu_2ZnSnSe_4$ solar cells fabricated by sputtering a Cu–Zn–Sn–Se quaternary compound target with a selenization process, J. Mater. Chem. A 7 (2019) 9948–9957.
[63] L. Yao, J. Ao, M.-J. Jeng, J. Bi, S. Gao, G. Sun, Q. He, Z. Zhou, Y. Sun, L.-B. Chang, CZTSe solar cell with 8.2% power conversion efficiency fabricated using electrodeposited Cu/Sn/Zn precursor and a three-step selenization process at low Se pressure, Sol. Energy Mater. Sol. Cells 159 (2017) 318–324.
[64] H. Ferhati, F. Djeffal, Role of intermediate metallic sub-layers in improving the efficiency of kesterite solar cells: concept and optimization, Mater. Res. Express 5 (2018) 036417, https://doi.org/10.1088/2053-1591/aab7ae
[65] H. Ferhati, F. Djeffal, Graded band-gap engineering for increased efficiency in CZTS solar cells, Opt. Mater. 76 (2018) 393–399, https://doi.org/10.1016/j.optmat.2018.01.006
[66] M.I. Hossain, A. Mohammad, W. Qarony, S. Ilhom, D.R. Shukla, D. Knipp, N. Biyikli, Y.H. Tsang, Atomic layer deposition of metal oxides for efficient perovskite single-junction and perovskite/silicon tandem solar cells, RSC Adv. 10 (2020) 14856–14866, https://doi.org/10.1039/D0RA00939C
[67] M.I. Hossain, A. Hongsingthong, W. Qarony, P. Sichanugrist, M. Konagai, A. Salleo, D. Knipp, Y.H. Tsang, Optics of perovskite solar cell front contacts, ACS Appl. Mater. Interfaces 11 (2019) 14693–14701, https://doi.org/10.1021/acsami.8b16586
[68] W. Qarony, M.I. Hossain, A. Tamang, V. Jovanov, A. Salleo, D. Knipp, Y.H. Tsang, Enhancing the energy conversion efficiency of low mobility solar cells by a 3D device architecture, J. Mater. Chem. C 7 (2019) 10289–10296, https://doi.org/10.1039/c9tc02358e